Supporting Information

A general method for precise modification of –O termination on MXenes by low-pressure flash annealing

Shi-Hao Yin,[a,#] Pei-Yu Cao,[a,#] Tianze Zhang,[b,#] Su-Fan Hu,[a] Ming-Ze Yang,[a] Hong-Yang Yuan,[a] Xu Xiao,[b,*] Li Zhang,[a,*] and Ye-Chuang Han.[a,*]

[a]Innovation Laboratory for Sciences and Technologies of Energy Materials of Fujian Province, State Key Laboratory of Physical Chemistry of Solid Surfaces, College of Chemistry and Chemical Engineering, Xiamen University, Xiamen 361005, P.R. China

[b]State Key Laboratory of Electronic Thin Film and Integrated Devices, School of Physics, University of Electronic Science and Technology of China, Chengdu 611731, P.R. China

[#]Contributed equally to this work.

*Corresponding author: ychan93@xmu.edu.cn; xuxiao@uestc.edu.cn;

zhangli81@xmu.edu.cn.

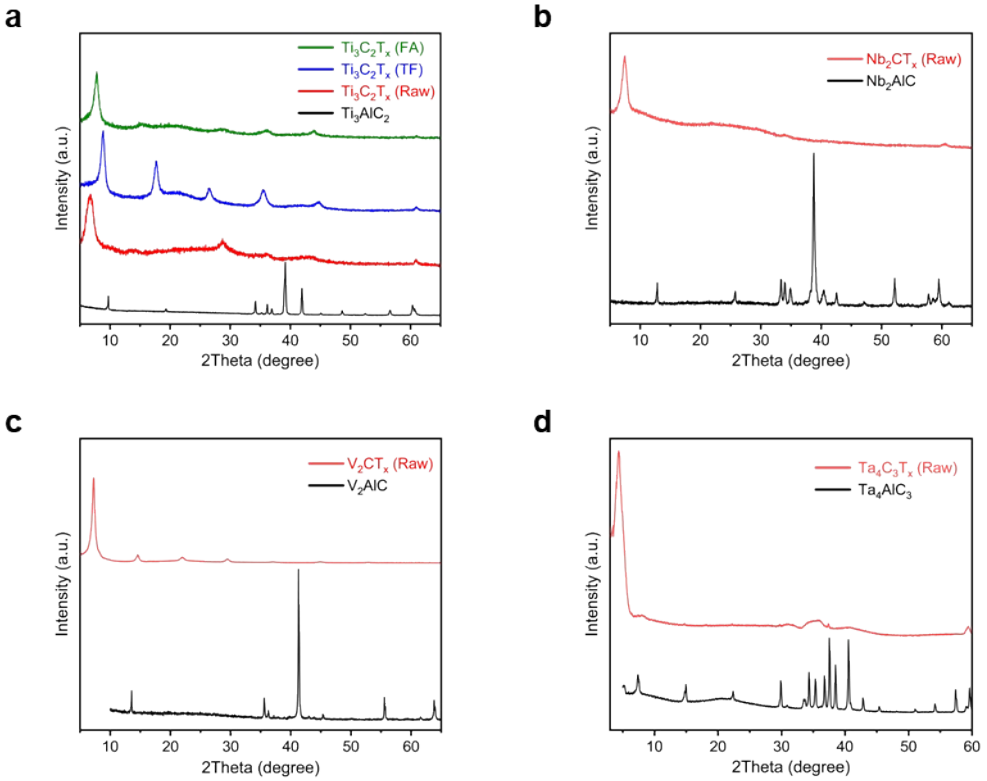

Fig. S1 XRD patterns of (**a**) Ti_3AlC_2, $Ti_3C_2T_x$ (Raw), $Ti_3C_2T_x$ (TF) and $Ti_3C_2T_x$ (FA), (**b**) Nb_2AlC and Nb_2CT_x (Raw), (**c**) V_2AlC and V_2CT_x (Raw), (**d**) Ta_4AlC_3 and $Ta_4C_3T_x$ (Raw).

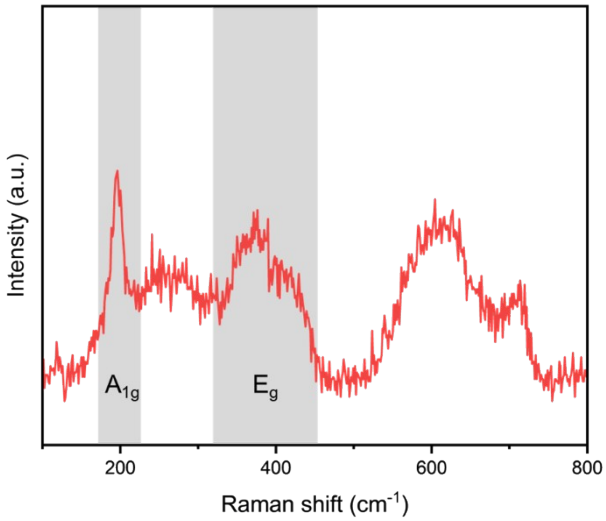

Fig. S2 Raman spectra of $Ti_3C_2T_x$ (Raw). The A_{1g} mode corresponds to the out-of-plane vibration of the surface terminations. E_g mode corresponds to the in-plane vibration of the surface terminations and outer Ti atoms.

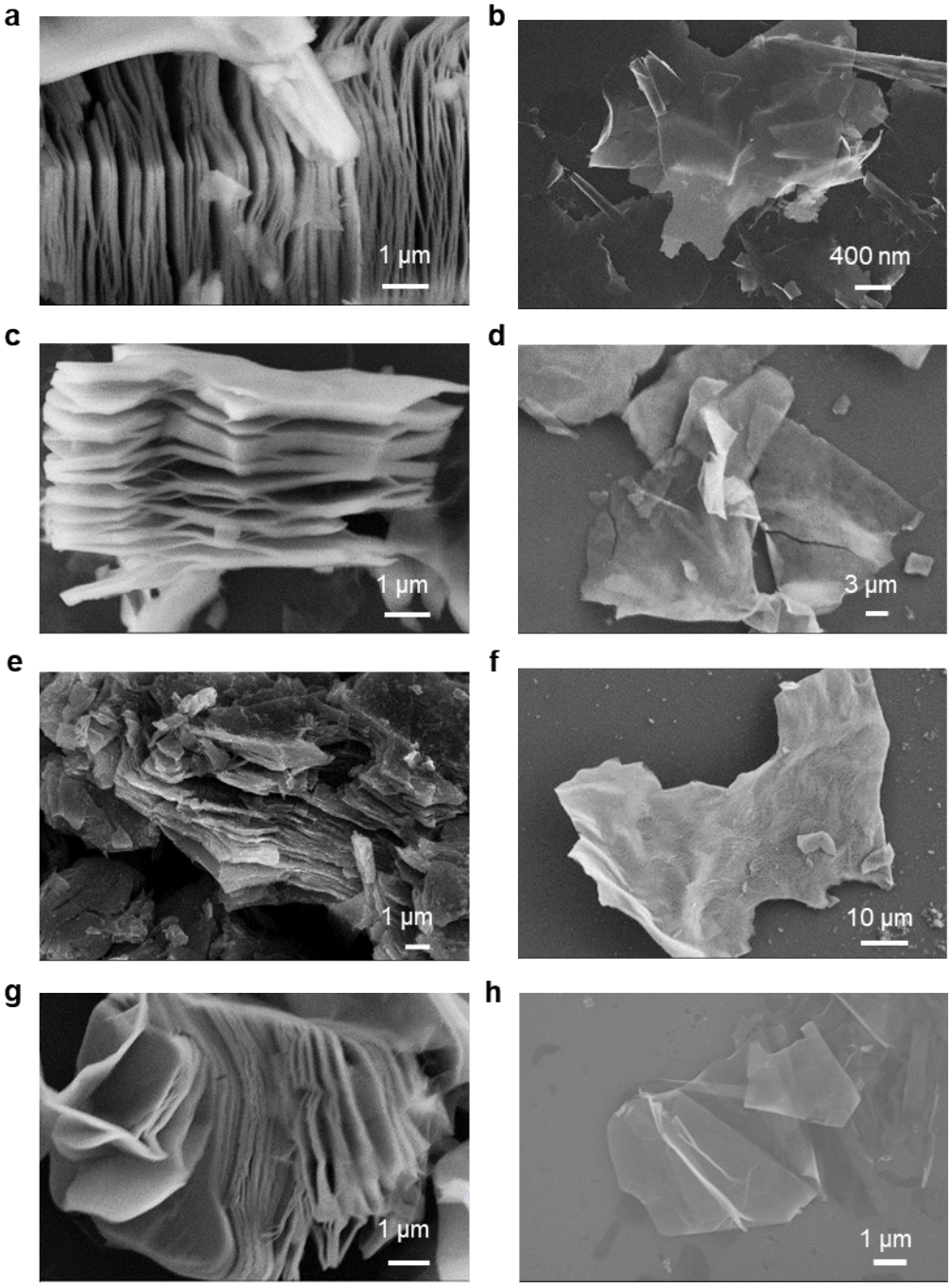

Fig. S3 SEM images of ML-MXene and corresponding MXene (Raw) (**a-b**) $Ti_3C_2T_x$, (**c-d**) Nb_2CT_x, (**e-f**) V_2CT_x and (**g-h**) $Ta_4C_3T_x$.

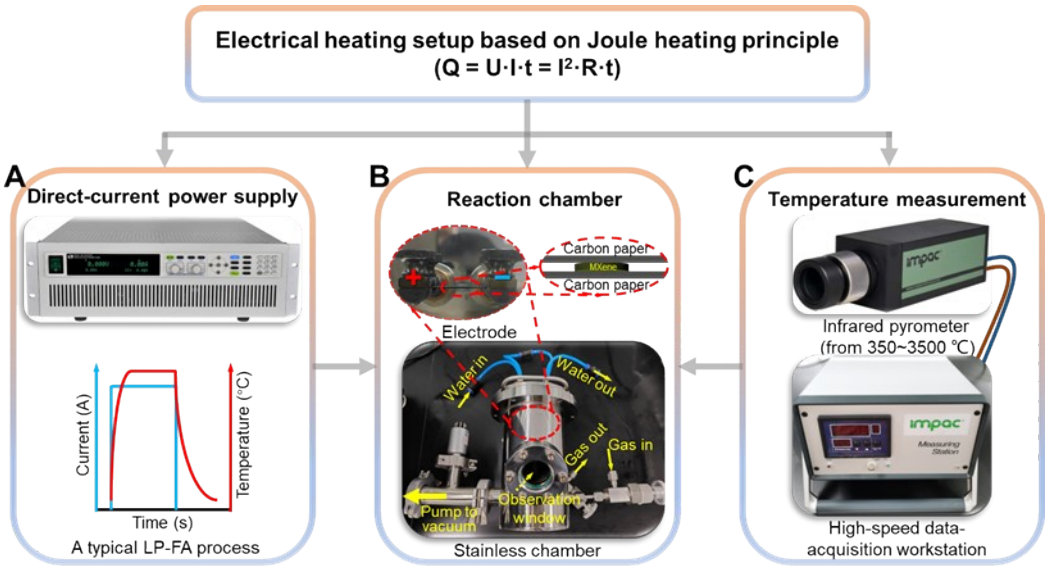

Fig. S4 The device of low-pressure flash annealing (LP-FA). Optical picture of (**a**) direct-current power supply, (**b**) Reaction chamber and (**c**) Temperature measurement.

(i) Direct-current power supply system with programmable-controlled pulse current delivery, capable of a maximum output of 240 A/80 V/6200 W. Typically, we usually fixed voltage and adjust current to control temperature.

(ii) Reaction chamber can not only provide vacuum reaction, which also accommodate various atmospheres, including Ar, N_2 and beyond. During a low-pressure flash annealing, a carbon paper/ MXene pellet/carbon paper structure was fixed to the copper electrodes, and a high temperature on carbon paper can be generated by the input of a pulse current under continuous vacuum pumping.

(iii) Temperature measurement system equip with infrared pyrometer (IMGA 740, IMPAC) and a high-speed data-acquisition workstation (one temperature point per microsecond), which can provide an accurately measure from 350 ℃ to 3500 ℃. That's important for monitoring the rapid temperature changes in low-pressure flash annealing.

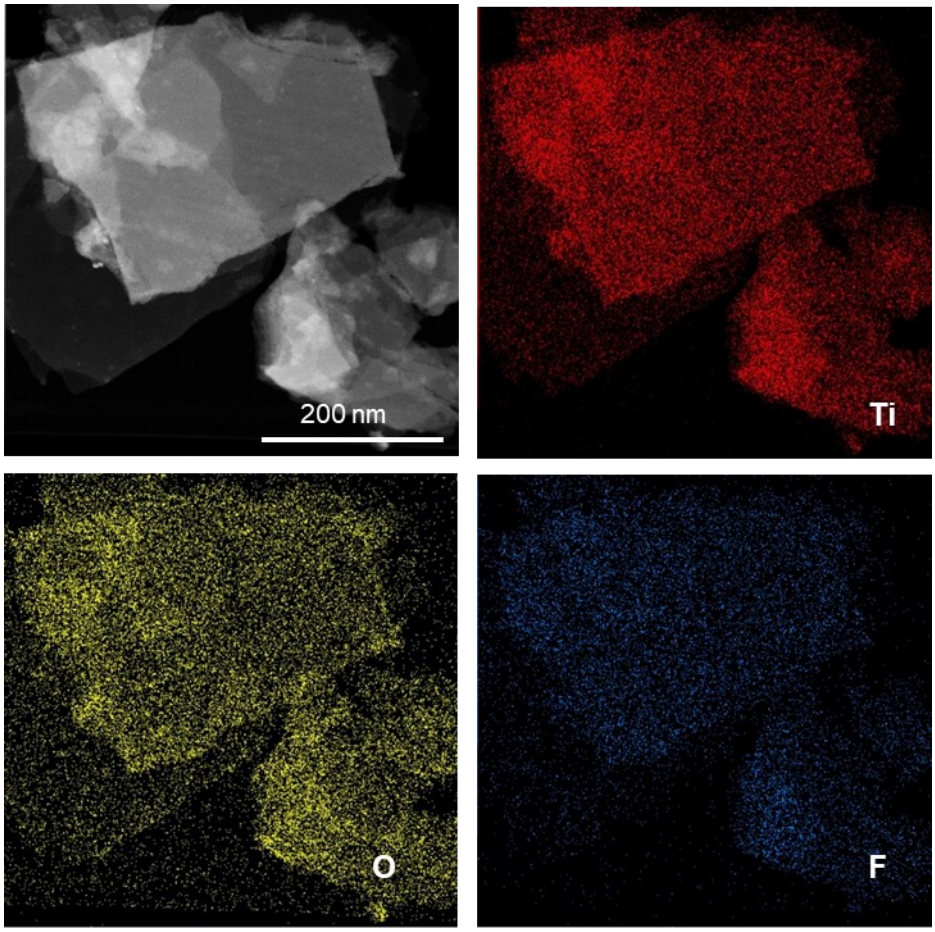

Fig. S5 HAADF-STEM images and corresponding EDS of $Ti_3C_2T_x$ (Raw).

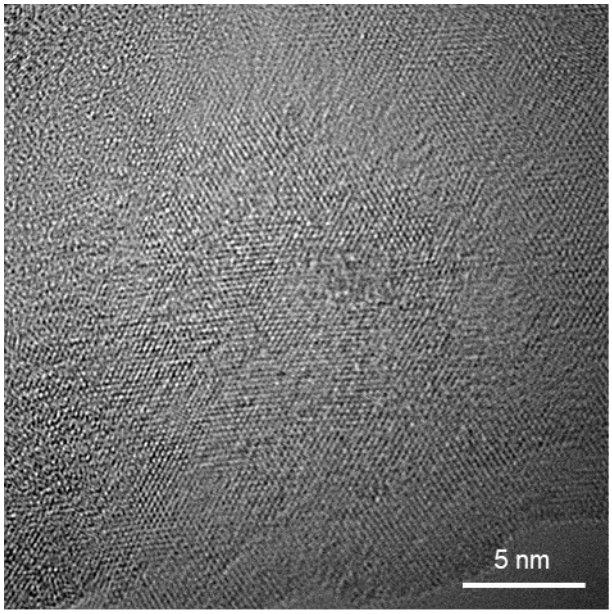

Fig. S6 High-resolution TEM of $Ti_3C_2T_x$ (LP-FA).

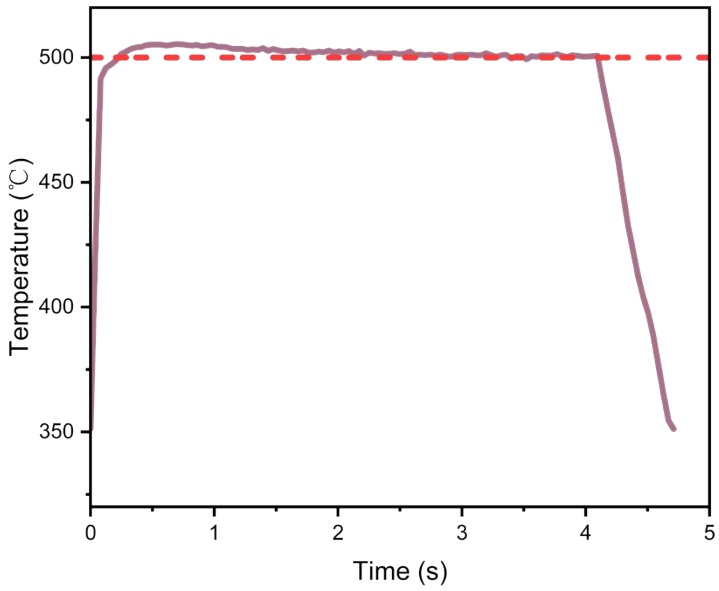

Fig. S7 The temperature and time profiles of LP-FA in the whole process.

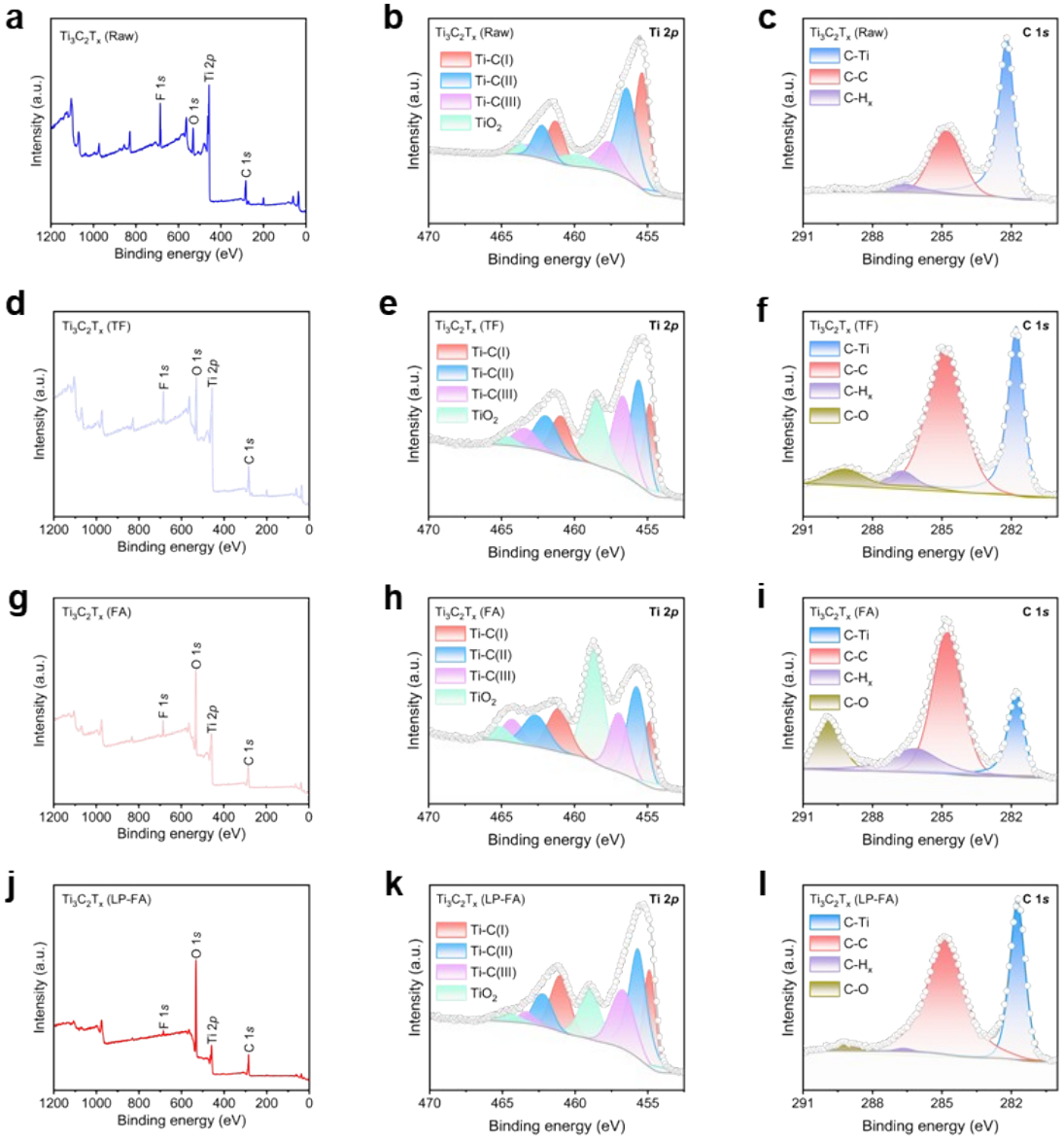

Fig. S8 XPS spectrum, High resolution XPS spectrum Ti 2*p* and C 1*s* of (**a-c**) $Ti_3C_2T_x$ (Raw), (**d-f**) $Ti_3C_2T_x$ (TF), (**g-i**) $Ti_3C_2T_x$ (FA) and (**j-l**) $Ti_3C_2T_x$ (LP-FA).

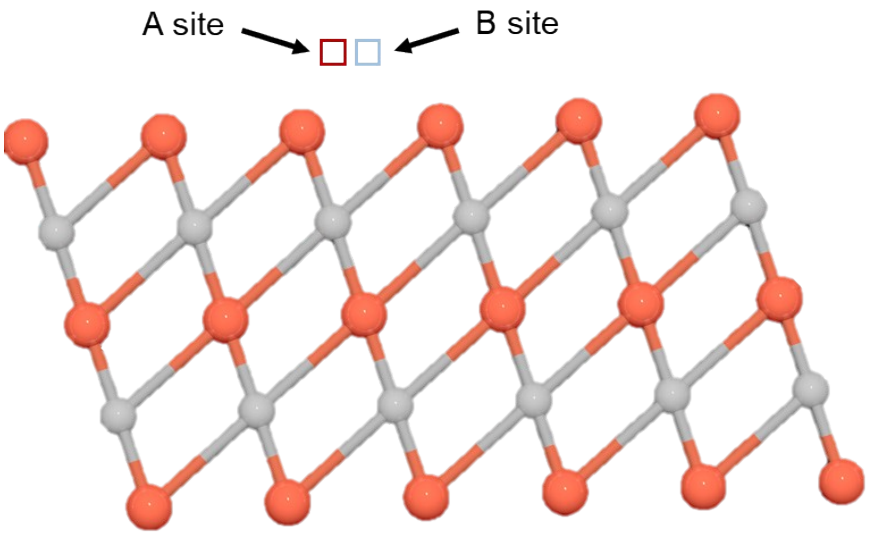

Fig. S9 The –O terminations occupy two adsorption sites on the T_3C_2 surface.

According to the previous works,[1, 2] in the High resolution XPS O 1*s* spectra (Fig. 3g), there are six peaks were fitted (Detailed peak information is shown in Table S6), two of which were assigned to –O terminations occupying different sites (A site and B site). The respective peaks were around in 530.0 eV and 531.9 eV.

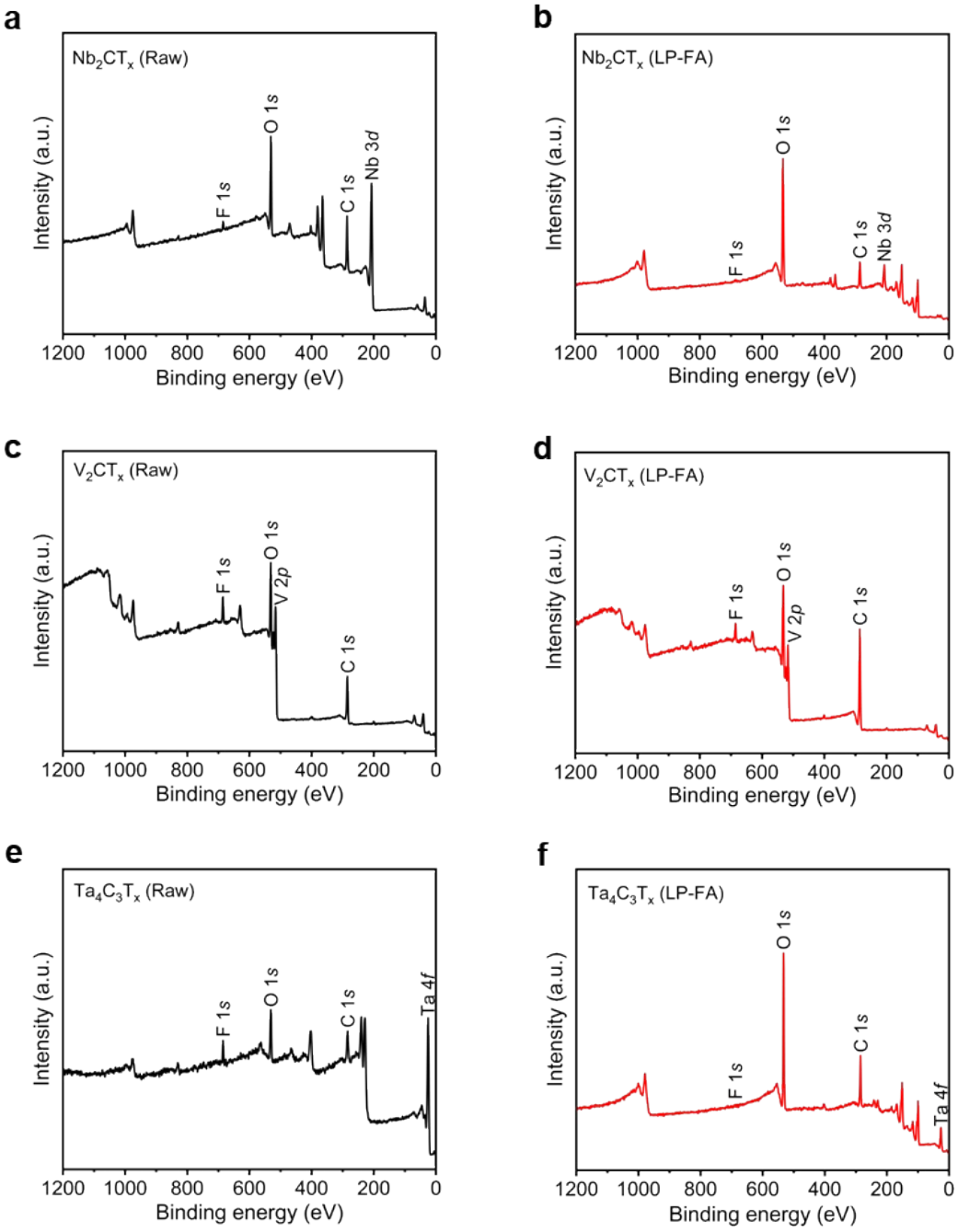

Fig. S10 XPS spectrum of (**a-b**) Nb_2CT_x (Raw) and Nb_2CT_x (LP-FA), (**c-d**) V_2CT_x (Raw) and V_2CT_x (LP-FA) and (**e-f**) $Ta_4C_3T_x$ (Raw) and $Ta_4C_3T_x$ (LP-FA).

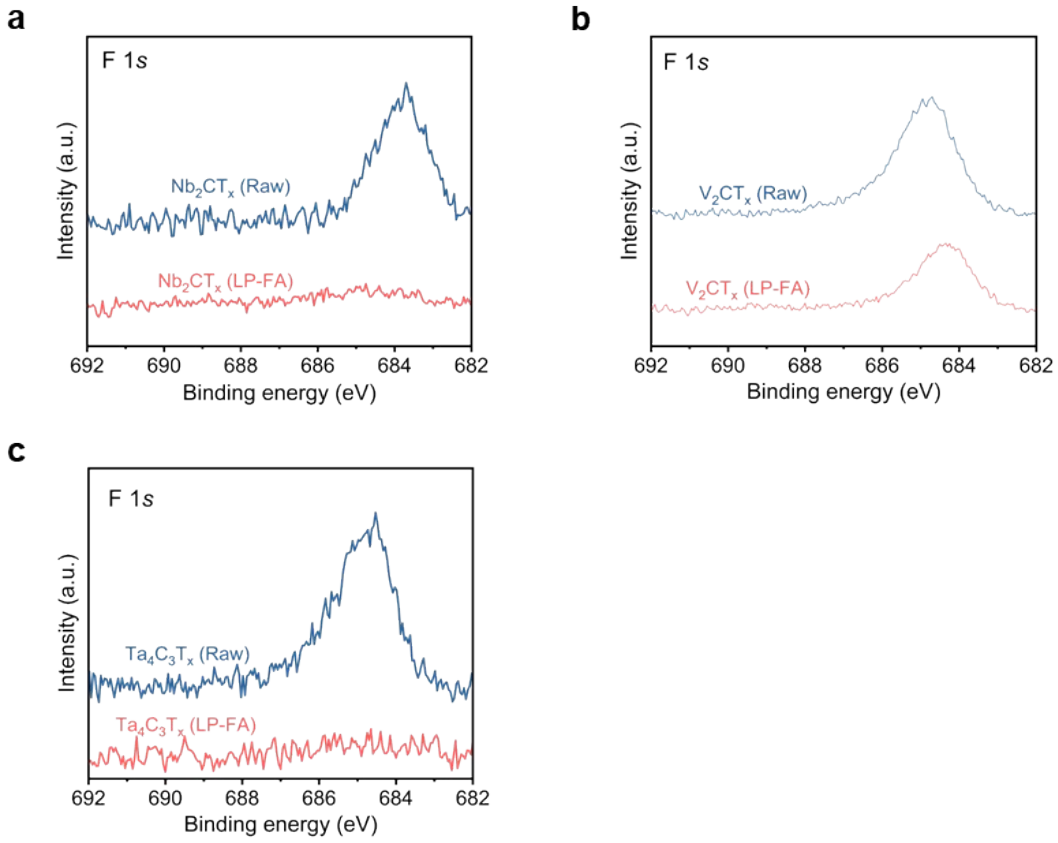

Fig. S11 High-resolution XPS F 1*s* of (**a**) Nb_2CT_x (Raw) and Nb_2CT_x (LP-FA), (**b**) V_2CT_x (Raw) and V_2CT_x (LP-FA), (**c**) $Ta_4C_3T_x$ (Raw) and $Ta_4C_3T_x$ (LP-FA).

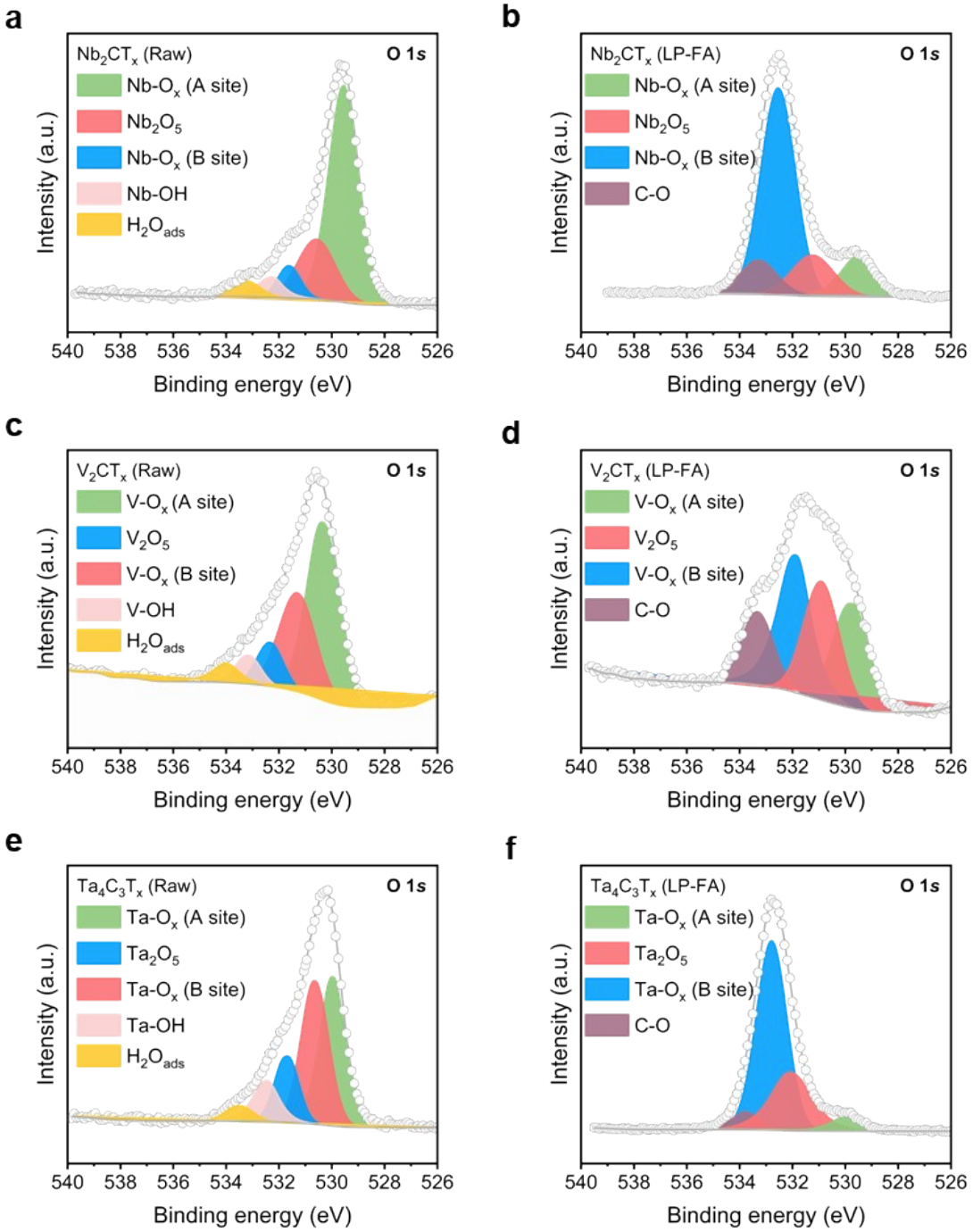

Fig. S12 High resolution XPS O 1*s* spectrum of (**a-b**) Nb_2CT_x (Raw) and Nb_2CT_x (LP-FA), (**c-d**) V_2CT_x (Raw) and V_2CT_x (LP-FA) and (**e-f**) $Ta_4C_3T_x$ (Raw) and $Ta_4C_3T_x$ (LP-FA).

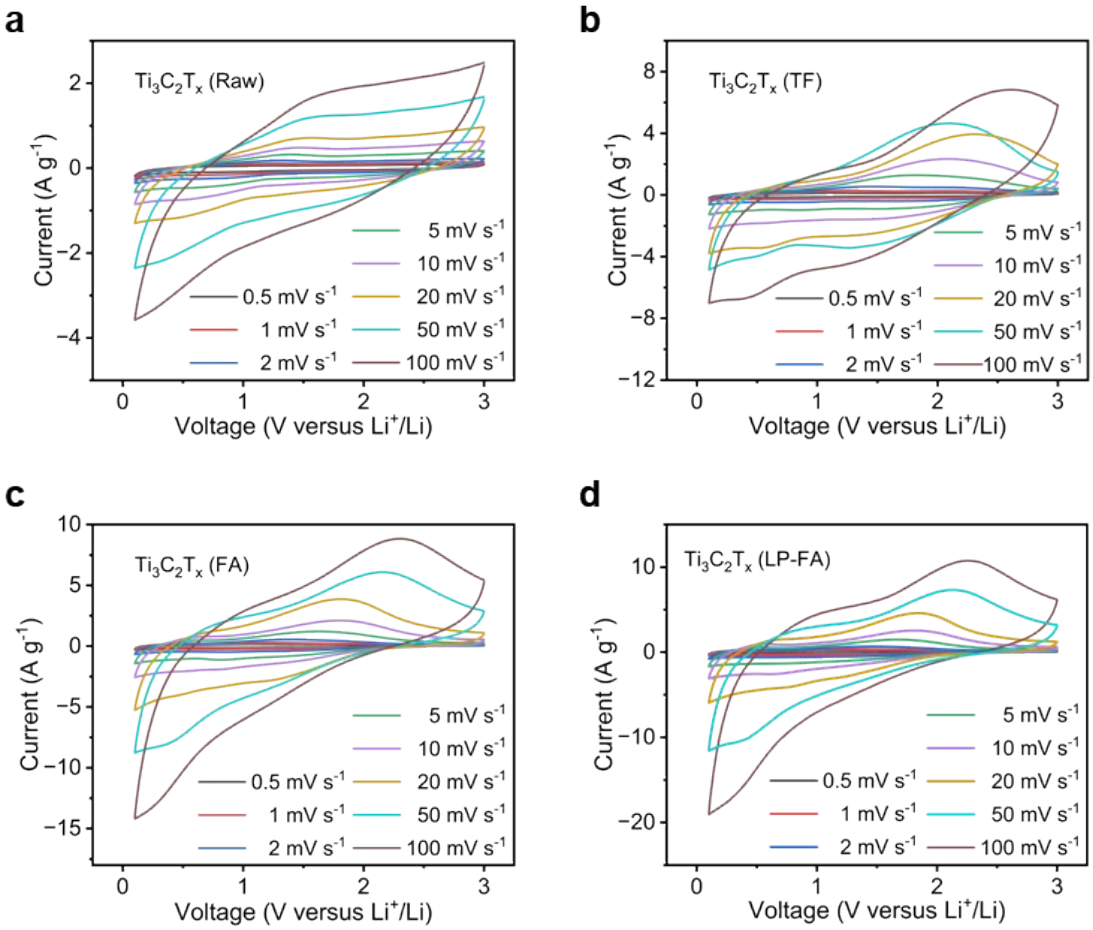

Fig. S13 CV profiles of (**a**) $Ti_3C_2T_x$ (Raw), (**b**) $Ti_3C_2T_x$ (TF), (**c**) $Ti_3C_2T_x$ (FA) and (**d**) $Ti_3C_2T_x$ (LP-FA) electrodes at scan rates from 0.5 to 100 mV s^{-1}.

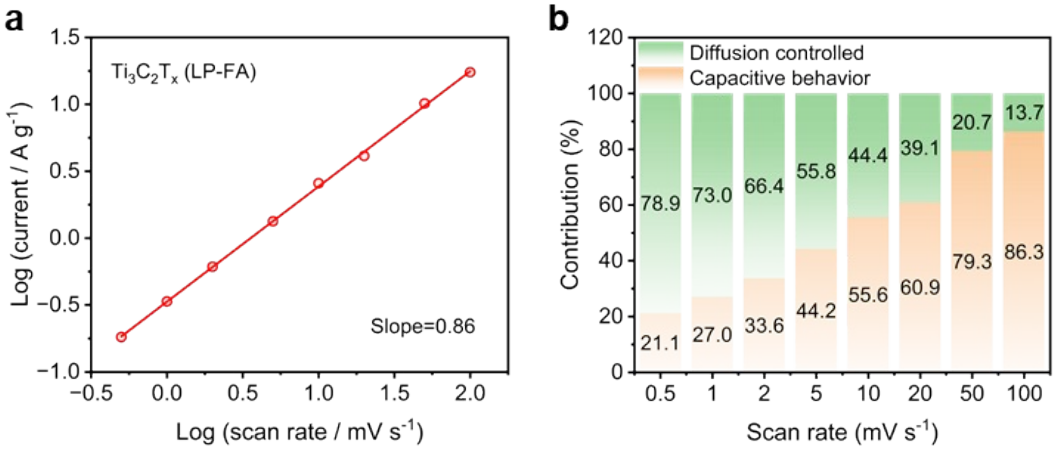

Fig. S14 Electrochemical energy storage properties of $Ti_3C_2T_x$ (LP-FA) electrode. (**a**) *b*-value determination of the peaks in CV profiles. (**b**) Capacitive contribution ratios at various scan rates.

The current (i) and the scan rate (v) obey a power-law relationship $i = av^b$, where a and b are adjustable constants.[3] The b-value can be determined by the slope of the log(v)-log(i) plots, which can be studied to distinguish the storage process of the charge. Specifically, b=0.5 indicates a diffusion-controlled process, while b=1 indicates a capacitive process. In our work, the calculated b-value is 0.86, indicating the mixed electrochemical storage process including diffusion-controlled and pseudocapacitive intercalations. Additionally, the total stored charge from capacitive processes could be quantified by deconvoluting the current response i at specific potentials (V) into capacitive effects (k_1v) and diffusion-controlled reactions (k_2v) according to $i = k_1v + k_2v$, where k_1 and k_2 are constants for a given potential.[4, 5] In our work, the diffusion-controlled contribution gradually decreases while the capacitive contribution gradually improves with increased scan rate from 0.5 mV s^{-1} to 100 mV s^{-1}. At 100 mV s^{-1}, the pseudocapacitive processes account for 86.3% of the charge storage.

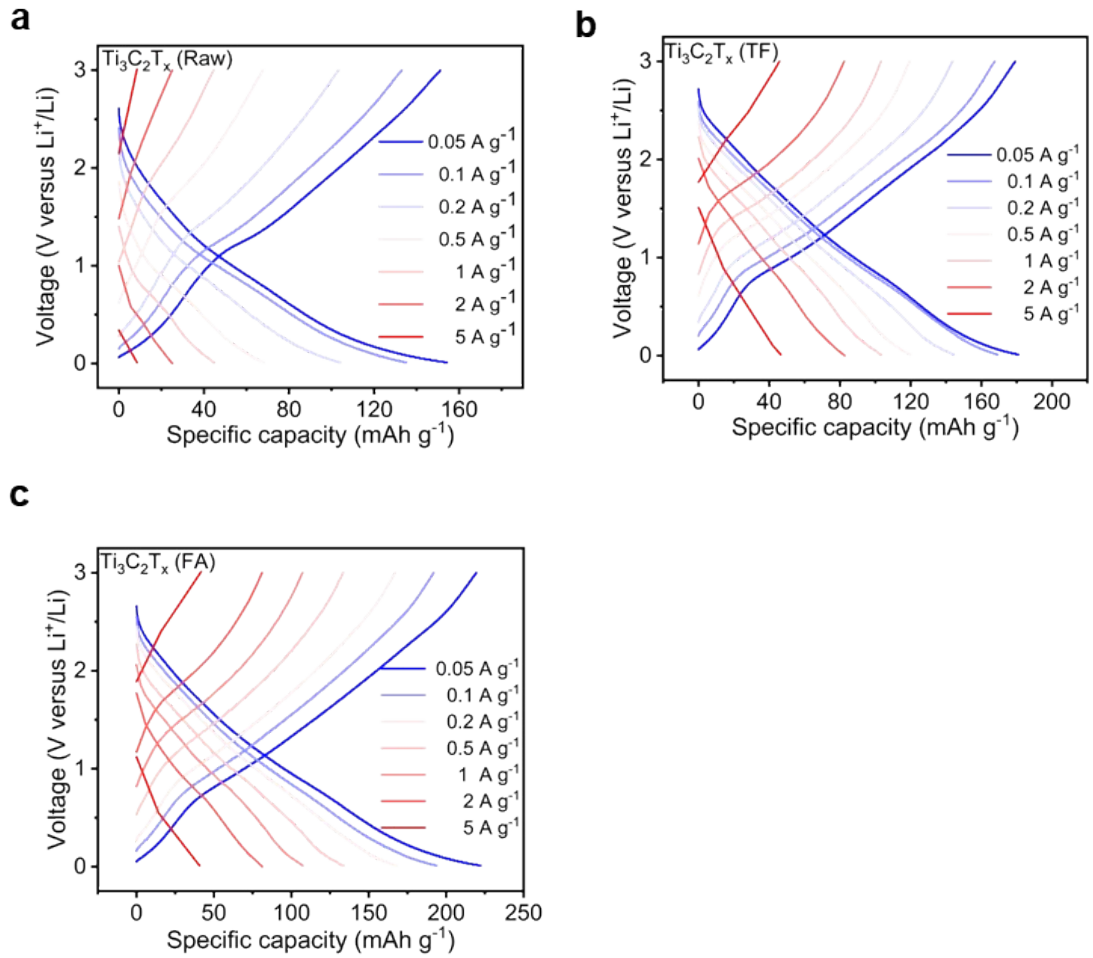

Fig. S15 Galvanostatic lithiation/delithiation profiles of (**a**) $Ti_3C_2T_x$ (Raw), (**b**) $Ti_3C_2T_x$ (TF), (**c**) $Ti_3C_2T_x$ (FA).

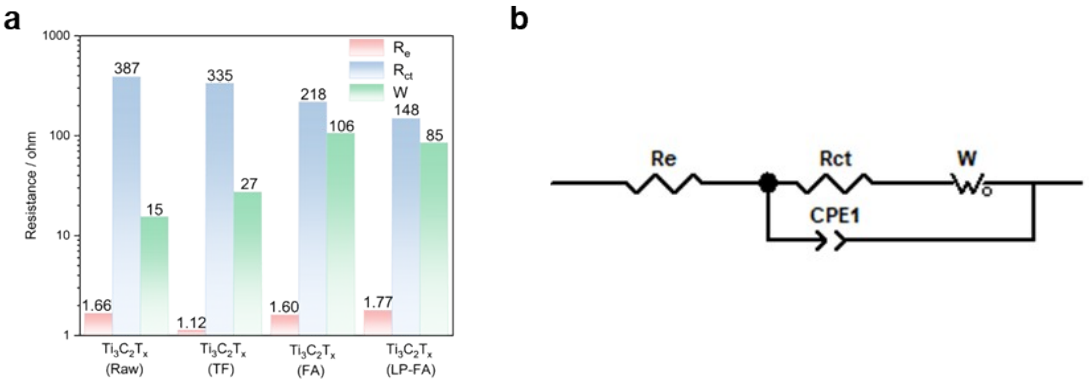

Fig. S16 The comparison of resistance values (**a**) and equivalent circuit diagram (**b**) of $Ti_3C_2T_x$ (Raw), $Ti_3C_2T_x$ (TF), $Ti_3C_2T_x$ (FA) and $Ti_3C_2T_x$ (LP-FA).

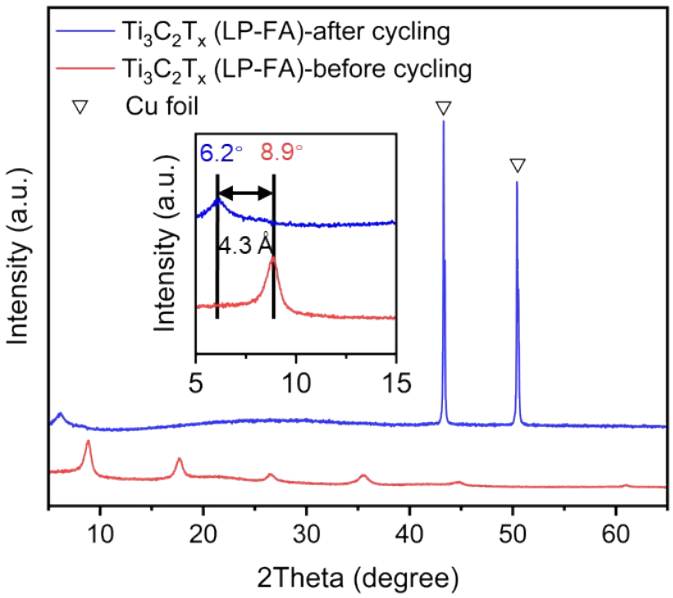

Fig. S17 XRD patterns of $Ti_3C_2T_x$ (LP-FA) before and after cycling, respectively.

The interlayer spacing of $Ti_3C_2T_x$ (LP-FA) increased from 9.9 Å (8.9°) to 14.2 Å (6.2°) after 3000 cycles at a current density of 3 A g^{-1}. This phenomenon could be ascribed to Li^+ repeatedly intercalated and deintercalated. The 43.3° and 50.4° peaks belong to the copper foil.

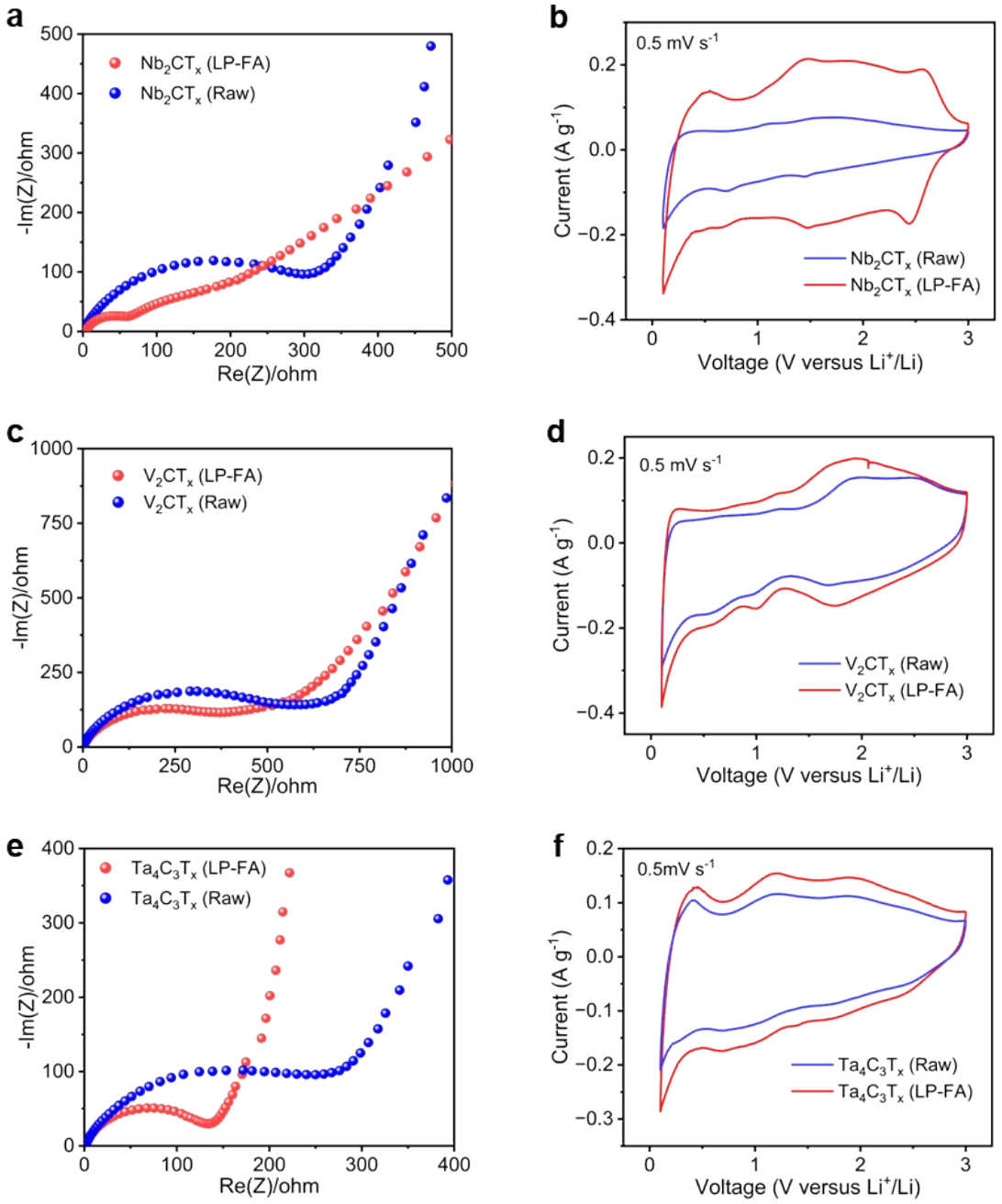

Fig. S18 Electrochemical impedance measurements and CV profiles of (**a-b**) Nb_2CT_x (Raw) and Nb_2CT_x (LP-FA), (**c-d**) V_2CT_x (Raw) and V_2CT_x (LP-FA), (**e-f**) $Ta_4C_3T_x$ (Raw) and $Ta_4C_3T_x$ (LP-FA).

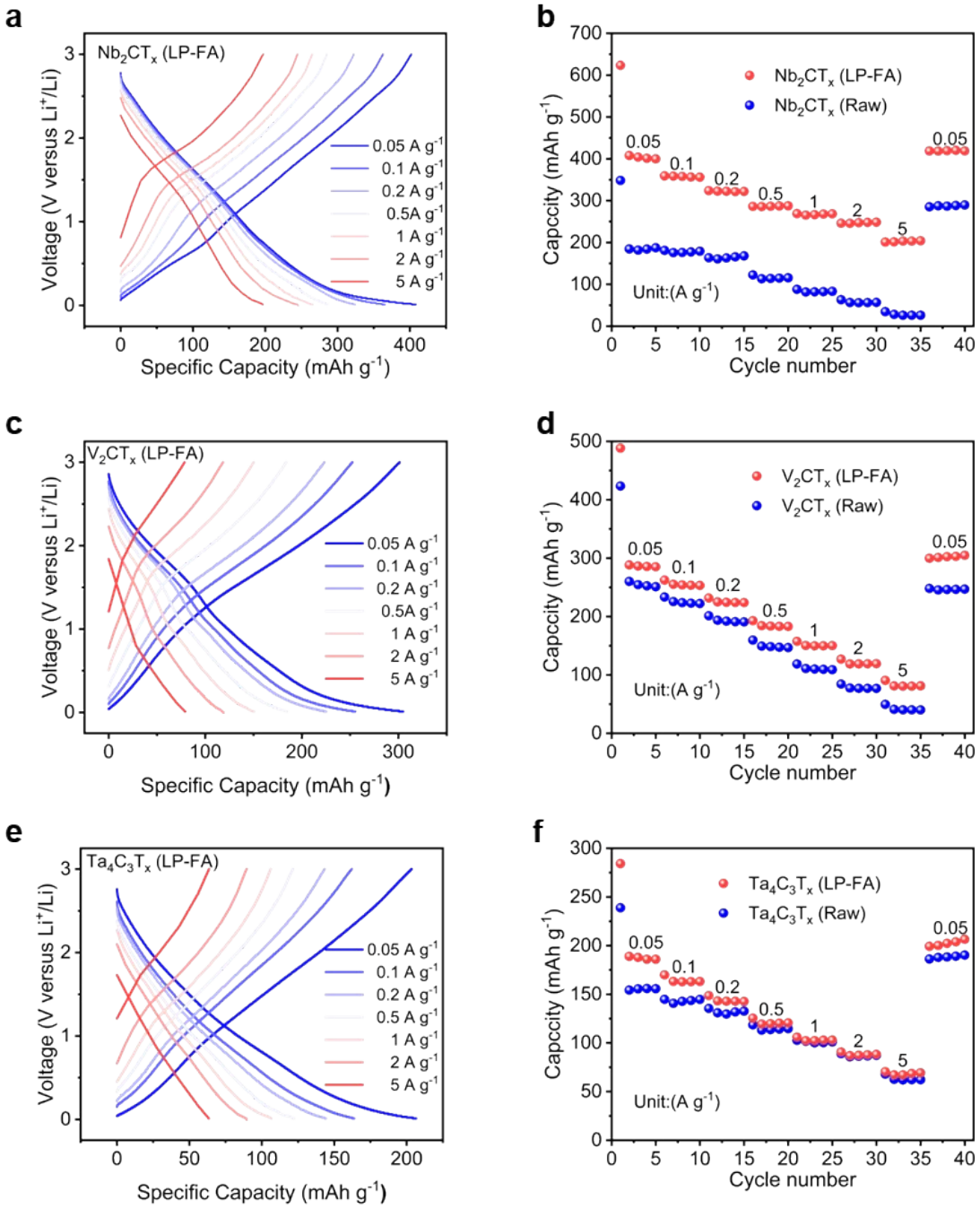

Fig. S19 Galvanostatic lithiation/delithiation profiles of (**a**) Nb_2CT_x (LP-FA), (**c**) V_2CT_x (LP-FA), (**e**) $Ta_4C_3T_x$ (LP-FA). (**b**) Rate capability of Nb_2CT_x (Raw) and Nb_2CT_x (LP-FA), (**d**) V_2CT_x (Raw) and V_2CT_x (LP-FA), (**f**) $Ta_4C_3T_x$ (Raw) and $Ta_4C_3T_x$ (LP-FA).

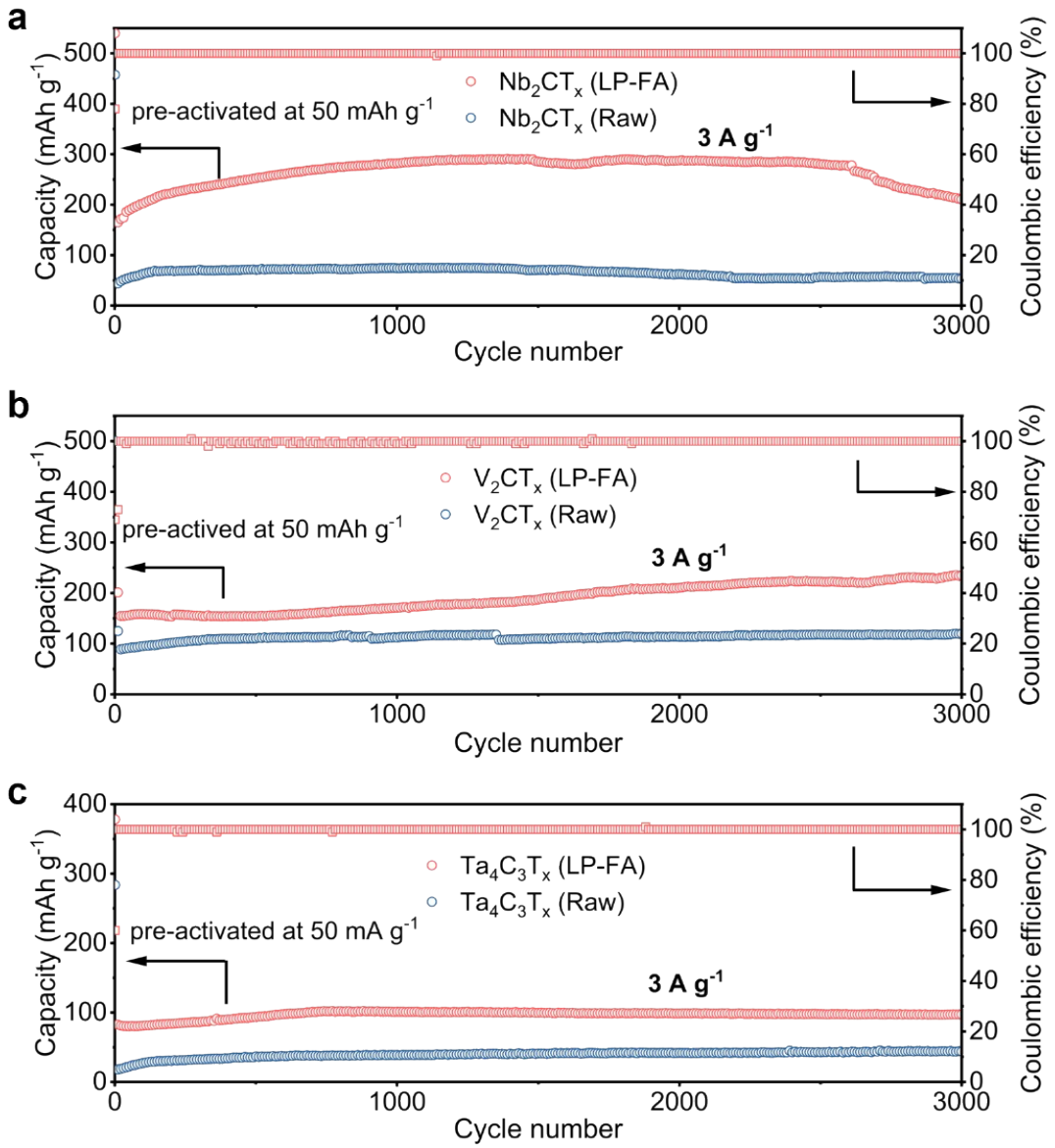

Fig. S20 The long cycling performance of (**a**) Nb_2CT_x (Raw) and Nb_2CT_x (LP-FA), (**b**) V_2CT_x (Raw) and V_2CT_x (LP-FA), (**c**) $Ta_4C_3T_x$ (Raw) and $Ta_4C_3T_x$ (LP-FA).

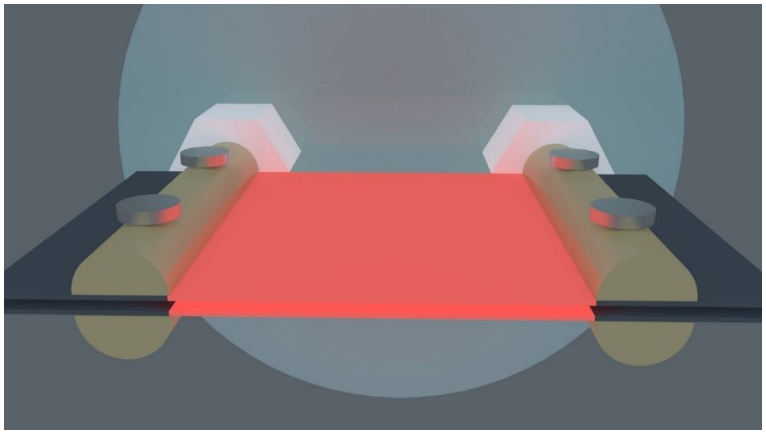

Fig. S21 Schematic of scaled-up high-temperature device.

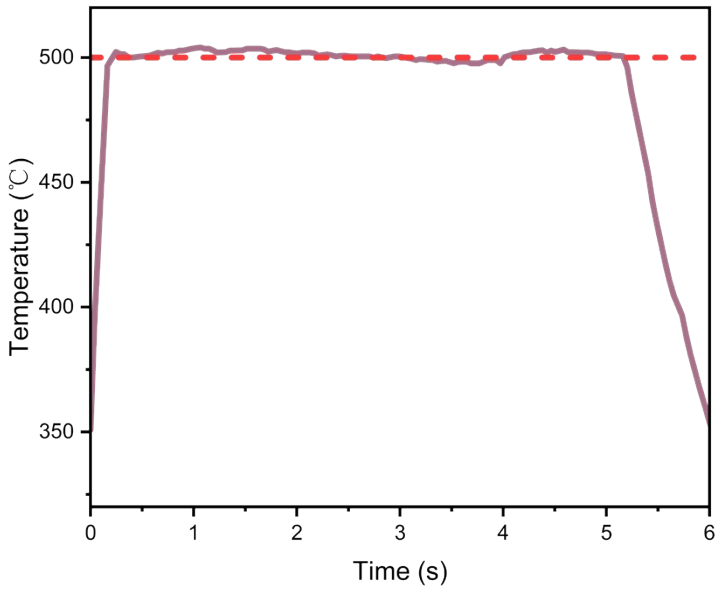

Fig. S22 The scaled-up high-temperature device temperature and time profiles of LP-FA in the whole process.

Fig. S23 Photograph of LA-$Ti_3C_2T_x$ (LP-FA) MXene film and corresponding weight.

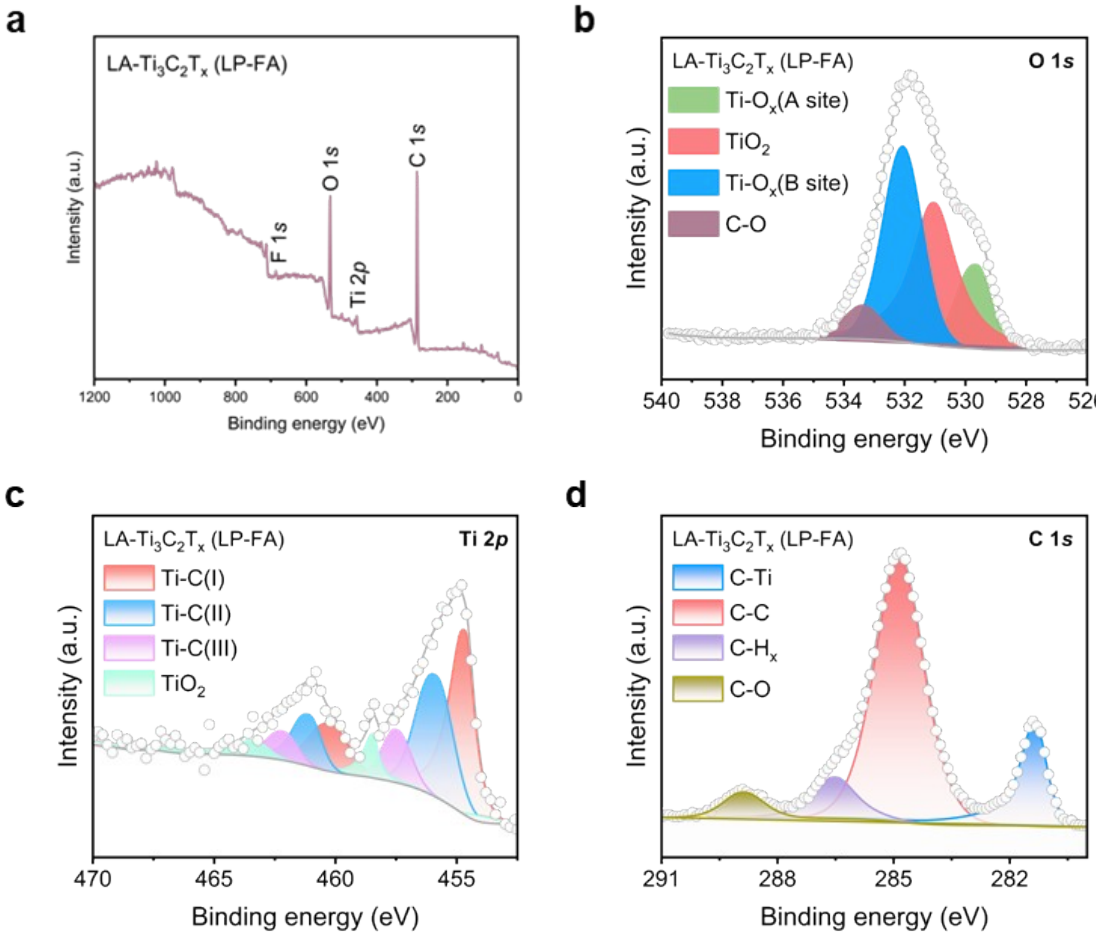

Fig. S24 XPS spectrum (**a**) and High-resolution XPS spectrum of O 1*s* (**b**) and Ti 2*p* (**c**) for LA-$Ti_3C_2T_x$ (LP-FA).

Table S1. Rietveld refinement results of $Ti_3C_2T_x$ (LP-FA), Nb_2CT_x (LP-FA), V_2CT_x (LP-FA), $Ta_4C_3T_x$ (LP-FA), LA-$Ti_3C_2T_x$ (LP-FA).

MXenes phase	Unit cell parameters/nm		Parameter	
	a	c	Rwp	GOF
$Ti_3C_2T_x$ (LP-FA)	0.294389	2.015782	5.500	1.20
Nb_2CT_x (LP-FA)	0.422529	1.163804	1.728	1.46
V_2CT_x (LP-FA)	0.401828	1.207834	2.015	1.44
$Ta_4C_3T_x$ (LP-FA)	0.315369	3.252352	2.799	2.51
LA-$Ti_3C_2T_x$ (LP-FA)	0.29375	2.012094	9.042	1.61

Table S2. Comparison of the heating duration and heating temperature in the various methods to obtain the O-terminated MXenes.

Materials	**Time**	***T* (°C)**	**Atmosphere**	**Methods**	**Ref.**
E-Ti_3C_2O	3 h	450	Ar	Tube furnace	6
F-Nb_2C	4 h	500	vacuum	Tube furnace	7
Annealed-$Ti_3C_2T_z$	20 min	400	Ar	Tube furnace	8
f-Ti_3C_2	40 h	500	Vacuum	Tube furnace	9
f-Nb_2C	40 h	400	vacuum	Tube furnace	
Ti_3C_2	30 min	500	H_2	Tube furnace	10
Ti_3C_2O	12-24 h	600	Ar	Molten salt	11
AD-$Ti_3C_2T_z$	20 min	400	Ar	Tube furnace	12
$Ti_3C_2T_x$	6 h	600	Ar	Tube furnace	13
V_2CO_2	4 h	400	vacuum	Tube furnace	14
O-Ti_3C_2	12 h	550	Ar	Molten salt	15
$Ti_3C_2T_x$	1 h	400	Ar	Tube furnace	16
$Ti_3C_2T_x$	10 h	500	Ar	Electric furnace	17
Nb_2CT_x	2 h	400	5% H_2/Ar	Tube furnace	18
$Ti_3C_2T_x$ (LP-FA)	**5 s**	**500**			
Nb_2CT_x (LP-FA)	**5 s**	**400**	**Low pressure**	**Flash**	**This**
V_2CT_x (LP-FA)	**5 s**	**400**	**(vacuum)**	**annealing**	**work**
$Ta_4C_3T_x$ (LP-FA)	**5 s**	**400**			

Table S3. The surface terminations atomic ratio (calculated by XPS spectrum) of $Ti_3C_2T_x$ (Raw), $Ti_3C_2T_x$ (TF), $Ti_3C_2T_x$ (FA) and $Ti_3C_2T_x$ (LP-FA).

Sample	**–OH (at.%)**	**–O (at.%)**	**–F (at.%)**	**H_2O_{ads} (at.%)**
$Ti_3C_2T_x$ (Raw)	3.9	34.2	49.5	12.4
$Ti_3C_2T_x$ (TF)	0	75.0	25.0	0
$Ti_3C_2T_x$ (FA)	0	89.0	11.0	0
$Ti_3C_2T_x$ (LP-FA)	0	97.4	2.6	0
LA-$Ti_3C_2T_x$ (LP-FA)	0	96.5	3.5	0

Table S4. High resolution XPS Ti 2*p* spectrum fitting results of $Ti_3C_2T_x$ (Raw), $Ti_3C_2T_x$ (TF), $Ti_3C_2T_x$ (FA) and $Ti_3C_2T_x$ (LP-FA).[19, 20]

Sample	BE (eV)	FWHM (eV)	Fraction	Assigned to
$Ti_3C_2T_x$ (Raw)	455.4 (461.3)	1.15 (1.35)	37.0	Ti-C(I)
	456.4 (462.2)	1.60 (1.40)	39.0	Ti-C(II)
	457.6 (463.0)	1.90 (1.10)	14.6	Ti-C(III)
	459.9 (463.8)	2.50 (1.50)	9.4	TiO_2
$Ti_3C_2T_x$ (TF)	454.9 (461.0)	0.90 (1.50)	23.0	Ti-C(I)
	455.6 (462.0)	1.30 (1.90)	31.5	Ti-C(II)
	456.7 (463.4)	1.60 (1.90)	24.9	Ti-C(III)
	458.5 (464.6)	1.65 (1.55)	20.6	TiO_2
$Ti_3C_2T_x$ (FA)	454.9 (461.0)	0.90 (1.75)	20.7	Ti-C(I)
	455.7 (462.7)	1.50 (2.00)	29.4	Ti-C(II)
	457.0 (464.2)	1.55 (1.55)	19.0	Ti-C(III)
	458.7 (465.1)	1.60 (1.60)	30.9	TiO_2
$Ti_3C_2T_x$ (LP-FA)	454.9 (461.0)	0.95 (1.50)	27.8	Ti-C(I)
	455.7 (462.2)	1.40 (1.55)	35.2	Ti-C(II)
	456.7 (463.4)	1.90 (1.40)	20.6	Ti-C(III)
	459.0 (464.7)	1.55 (2.00)	16.4	TiO_2
LA-$Ti_3C_2T_x$ (LP-FA)	454.7 (460.2)	1.20 (1.90)	41.3	Ti-C(I)
	455.9 (461.1)	1.80 (1.40)	34.4	Ti-C(II)
	457.5 (462.2)	1.40 (1.45)	13.5	Ti-C(III)
	458.5 (463.4)	0.70 (1.60)	10.8	TiO_2

BE: Binding energy

Table S5. High resolution XPS C 1*s* spectrum fitting results of $Ti_3C_2T_x$ (Raw), $Ti_3C_2T_x$ (TF), $Ti_3C_2T_x$ (FA) and $Ti_3C_2T_x$ (LP-FA).[19, 20]

Sample	BE (eV)	FWHM (eV)	Fraction	Assigned to
$Ti_3C_2T_x$ (Raw)	282.2	0.8	58.5	C-Ti
	284.8	1.6	35.0	C-C
	286.6	1.6	6.5	C-H_x
$Ti_3C_2T_x$ (TF)	281.8	0.8	35.0	C-Ti
	284.8	1.8	55.0	C-C
	286.7	1.2	4.0	C-H_x
	289.2	1.8	6.0	C-O
$Ti_3C_2T_x$ (FA)	281.8	0.8	49.5	C-Ti
	284.8	1.5	19.0	C-C
	286.1	2.4	15.5	C-H_x
	289.9	1.3	16.0	C-O
$Ti_3C_2T_x$ (LP-FA)	281.8	0.8	35.5	C-Ti
	284.8	1.8	62.5	C-C
	286.6	0.8	0.5	C-H_x
	289.2	1.1	1.5	C-O
LA-$Ti_3C_2T_x$ (LP-FA)	281.3	0.8	18.5	C-Ti
	284.8	1.5	66.5	C-C
	286.5	1.3	10.0	C-H_x
	288.9	1.0	5.0	C-O

Table S6. High resolution XPS O 1*s* spectrum fitting results of $Ti_3C_2T_x$ (Raw), $Ti_3C_2T_x$ (TF), $Ti_3C_2T_x$ (FA) and $Ti_3C_2T_x$ (LP-FA).

Sample	BE (eV)	FWHM (eV)	Fraction	Assigned to
$Ti_3C_2T_x$ (Raw)	530.0	1.1	48.6	C-Ti-O_x (A site)
	531.0	1.1	11.9	TiO_2
	531.9	1.1	11.0	C-Ti-O_x (B site)
	532.7	1.7	6.8	C-Ti-OH
	533.5	1.7	21.7	H_2O_{ads}
$Ti_3C_2T_x$ (TF)	529.7	1.0	31.2	C-Ti-O_x (A site)
	530.4	1.2	33.8	TiO_2
	531.5	1.4	14.4	C-Ti-O_x (B site)
	532.2	1.3	11.0	C-O
	533.4	1.8	9.6	H_2O_{ads}
$Ti_3C_2T_x$ (FA)	529.7	1.1	18.9	C-Ti-O_x (A site)
	530.4	1.3	29.4	TiO_2
	531.7	1.5	45.7	C-Ti-O_x (B site)
	532.9	1.9	6.0	C-O
$Ti_3C_2T_x$ (LP-FA)	529.6	1.1	7.5	C-Ti-O_x (A site)
	530.4	1.6	22.1	TiO_2
	531.8	1.3	63.7	C-Ti-O_x (B site)
	532.9	1.4	6.7	C-O
LA-$Ti_3C_2T_x$ (LP-FA)	529.7	1.3	15.7	C-Ti-O_x (A site)
	531.0	1.7	39.0	TiO_2
	532.0	1.5	39.1	C-Ti-O_x (B site)
	533.4	1.4	6.2	C-O

Table S7. The surface terminations atomic ratio (calculated by XPS spectrum) of Nb_2CT_x (Raw) and Nb_2CT_x (LP-FA), V_2CT_x (Raw) and V_2CT_x (LP-FA), $Ta_4C_3T_x$ (Raw) and $Ta_4C_3T_x$ (LP-FA).

Sample	–OH (at.%)	–O (at.%)	–F (at.%)	H_2O_{ads} (at.%)
Nb_2CT_x (Raw)	6.5	80.6	6.4	6.5
Nb_2CT_x (LP-FA)	0	100.0	0	0
V_2CT_x (Raw)	5.4	72	18.9	3.7
V_2CT_x (LP-FA)	0	89.1	10.9	0
$Ta_4C_3T_x$ (Raw)	13.1	62.9	21.3	2.7
$Ta_4C_3T_x$ (LP-FA)	0	100.0	0	0

Table S8. High resolution XPS O 1*s* spectrum fitting results of Nb_2CT_x (Raw) and Nb_2CT_x (LP-FA), V_2CT_x (Raw) and V_2CT_x (LP-FA), $Ta_4C_3T_x$ (Raw) and $Ta_4C_3T_x$ (LP-FA).

Sample	BE (eV)	FWHM (eV)	Fraction	Assigned to
Nb_2CT_x (Raw)	529.6	1.3	61.5	C-Nb-O_x (A site)
	530.6	1.7	20.8	Nb_2O_5
	531.6	1.0	6.7	C-Nb-O_x (B site)
	532.2	1.2	5.5	C-Nb-OH
	533.3	1.4	5.5	H_2O_{ads}
Nb_2CT_x (LP-FA)	529.5	1.5	13.2	C-Nb-O_x (A site)
	531.2	1.8	14.6	Nb_2O_5
	532.5	1.5	61.4	C-Nb-O_x (B site)
	533.3	1.6	10.8	C-O
V_2CT_x (Raw)	530.3	1.4	49.4	C-V-O_x (A site)
	531.1	1.6	30.1	V_2O_5
	532.3	1.12	9.5	C-V-O_x (B site)
	533.2	1.1	6.0	C-V-OH
	534.0	1.2	5.2	H_2O_{ads}
V_2CT_x (LP-FA)	529.7	1.6	24.6	C-V-O_x (A site)
	530.9	1.6	27.5	V_2O_5
	531.9	1.5	32.8	C-V-O_x (B site)
	533.3	1.4	15.2	C-O
$Ta_4C_3T_x$ (Raw)	530.0	1.1	30.8	C-Ta-O_x (A site)
	530.6	1.2	29.7	Ta_2O_5

	531.7	1.1	11.9	C-Ta-O_x (B site)
	532.5	1.2	9.1	C-Ta-OH
	533.5	1.2	3.2	H_2O_{ads}
$Ta_4C_3T_x$ (LP-FA)	530.0	1.3	5.3	C-Ta-O_x (A site)
	532.0	18	27.0	Ta_2O_5
	532.8	1.4	62.3	C-Ta-O_x (B site)
	533.8	1.2	5.4	C-O

Table S9. The EDS analyses of $Ti_3C_2T_x$ (Raw) and various $Ti_3C_2T_x$ (LP-FA) under different reaction temperature and time conditions.

Sample	**Element (wt.%)**			
	Ti	C	O	F
$Ti_3C_2T_x$ (Raw)	63.69	12.56	8.57	15.18
$Ti_3C_2T_x$ (LP-FA) 400 ℃-5 s	55.67	16.89	19.51	7.93
$Ti_3C_2T_x$ (LP-FA) 500 ℃-3 s	67.63	15.80	11.35	5.22
$Ti_3C_2T_x$ (LP-FA) 500 ℃-5 s	53.64	18.74	27.00	0.62
$Ti_3C_2T_x$ (LP-FA) 600 ℃-5 s	64.61	14.92	19.08	1.39

Table S10. Li^+ storage capacities of $Ti_3C_2T_x$ (Raw) electrode at different scan rates.

Scan rate / mV s^{-1}	**Capacitance / F g^{-1}**	**Capacity / mAh g^{-1}**	**Time / min (C-rate)**	**Coulombic efficiency / %**
0.5	106	85	96.7 (0.6)	100.0
1	89	71	48.3 (1.2)	98.5
2	66	53	24.2 (2.5)	99.6
5	46	37	9.7 (6.2)	99.4
10	34	28	4.8 (12.4)	99.7
20	25	20	2.4 (24.8)	102.3
50	16	13	0.97 (62.1)	102.6
100	11	9	0.48 (124.1)	101.2

Table S11. Li^+ storage capacities of $Ti_3C_2T_x$ (TF) electrode at different scan rates.

Scan rate / mV s^{-1}	**Capacitance / F g^{-1}**	**Capacity / mAh g^{-1}**	**Time / min (C-rate)**	**Coulombic efficiency / %**
0.5	187	150	96.7 (0.6)	95.7
109	92	146	48.3 (1.2)	97.9
2	164	132	24.2 (2.5)	99.8
5	135	109	9.7 (6.2)	100.0
10	115	92	4.8 (12.4)	99.8
20	92	74	2.4 (24.8)	99.2
50	44	36	0.97 (62.1)	99.7
100	28	23	0.48 (124.1)	99.4

Table S12. Li^+ storage capacities of $Ti_3C_2T_x$ (FA) electrode at different scan rates.

Scan rate / mV s^{-1}	**Capacitance / F g^{-1}**	**Capacity / mAh g^{-1}**	**Time / min (C-rate)**	**Coulombic efficiency / %**
0.5	173	139	96.7 (0.6)	99.4
1	156	126	48.3 (1.2)	100.5
2	139	112	24.2 (2.5)	99.4
5	120	96	9.7 (6.2)	99.9
10	103	83	4.8 (12.4)	100.2
20	91	73	2.4 (24.8)	100.2
50	57	46	0.97 (62.1)	100.2
100	39	32	0.48 (124.1)	100.2

Table S13. Li^+ storage capacities of $Ti_3C_2T_x$ (LP-FA) electrode at different scan rates.

Scan rate / mV s^{-1}	**Capacitance / F g^{-1}**	**Capacity / mAh g^{-1}**	**Time / min (C-rate)**	**Coulombic efficiency / %**
0.5	200	161	96.7 (0.6)	98.7
1	185	150	48.3 (1.2)	98.3
2	165	133	24.2 (2.5)	99.5
5	138	112	9.7 (6.2)	100.0
10	120	96	4.8 (12.4)	100.3
20	101	82	2.4 (24.8)	99.2
50	70	56	0.97 (62.1)	100.6
100	50	41	0.48 (124.1)	100.1

Table S14. Electrochemical performance of reported MXenes and commercial graphite as compared to MXenes (LP-FA).

Materials	Current density (A/g)	Specific capacity (mAh/g)	Cycle numbers	Ref.
$Ti_3C_2T_x$	1	82	1000	21
in-$Ti_3C_2T_x$	2.6	88	100	22
NH_3-$Ti_3C_2T_x$	0.32	168	500	23
LB-$Ti_3C_2T_x$	3	120	3000	24
na- $Ti_3C_2T_x$	0.5	104.8	500	25
p-MXene-71	1	215.6	3500	26
	2	187.4	3500	
AD-$Ti_3C_2T_z$	1	89	2000	12
$Ti_3C_2T_z$ nanosheets	1	300	1000	27
Ti_3C_2@400 °C	1 C	126.4	100	28
e-MS- $Ti_3C_2T_x$	4	85	2000	29
Graphite	0.2 C	218		30
	0.5 C	196		
	1 C	179		
	2 C	175		
	5 C	149		
$Ti_3C_2T_x$ (LP-FA)	**3**	**266.4**	**3000**	**This work**
Nb_2CT_x (LP-FA)	**3**	**210.6**	**3000**	
V_2CT_x (LP-FA)	**3**	**234.6**	**3000**	
$Ta_4C_3T_x$ (LP-FA)	**3**	**97.2**	**3000**	

References

1. V. Natu, M. Benchakar, C. Canaff, A. Habrioux, S. Célérier and M. W. Barsoum, *Matter*, 2021, **4**, 1224-1251.
2. I. Persson, L.-Å. Näslund, J. Halim, M. W. Barsoum, V. Darakchieva, J. Palisaitis, J. Rosen and P. O. Å. Persson, *2D Mater.*, 2018, **5**, 015002.
3. V. Augustyn, J. Come, M. A. Lowe, J. W. Kim, P.-L. Taberna, S. H. Tolbert, H. D. Abruña, P. Simon and B. Dunn, *Nat. Mater.*, 2013, **12**, 518-522.
4. L. Shen, S. Chen, J. Maier and Y. Yu, *Adv. Mater.*, 2017, **29**, 1701571.
5. Z. Hu, J. Liu, X. Zhao, X. Zhan, H. Wang, H. Yang, J. Wu, X. Fang, Q. Zhang, J. Liu and L. Zhang, *Adv. Funct. Mater.*, 2024, **34**, 2402199.
6. Y. Jiang, T. Sun, X. Xie, W. Jiang, J. Li, B. Tian and C. Su, *ChemSusChem*, 2019, **12**, 1368-1373.
7. J. Li, X. Yuan, C. Lin, Y. Yang, L. Xu, X. Du, J. Xie, J. Lin and J. Sun, *Adv. Energy Mater.*, 2017, **7**, 1602725.
8. L. Cai, Z. Li, S. Zhang, K. Prenger, M. Naguib and V. G. Pol, *Chem. Eng. J.*, 2021, **419**, 129387.
9. Y. Xie, M. Naguib, V. N. Mochalin, M. W. Barsoum, Y. Gogotsi, X. Yu, K.-W. Nam, X.-Q. Yang, A. I. Kolesnikov and P. R. C. Kent, *J. Am. Chem. Soc.*, 2014, **136**, 6385-6394.
10. M. Lu, H. Li, W. Han, J. Chen, W. Shi, J. Wang, X.-M. Meng, J. Qi, H. Li, B. Zhang, W. Zhang and W. Zheng, *J. Energy Chem.*, 2019, **31**, 148-153.
11. V. Kamysbayev, A. S. Filatov, H. Hu, X. Rui, F. Lagunas, D. Wang, R. F. Klie and D. V. Talapin, *Science*, 2020, **369**, 979-983.
12. Y. Li, S. Arnold, S. Husmann and V. Presser, *J. Energy Storage*, 2023, **60**, 106625.
13. A. Gentile, C. Ferrara, S. Tosoni, M. Balordi, S. Marchionna, F. Cernuschi, M.-H. Kim, H.-W. Lee and R. Ruffo, *Small Methods*, 2020, **4**, 2000314.
14. H. Xu, R. Zheng, D. Du, L. Ren, R. Li, X. Wen, C. Zhao and C. Shu, *Appl. Mater. Today.*, 2022, **27**, 101464.
15. L. Liu, E. Raymundo-Piñero, S. Sunny, P.-L. Taberna and P. Simon, *Angew. Chem. Int. Ed.*, 2024, **63**, e202319238.
16. S. Song, F. Yin, Y. Fu, J. Ren, J. Ma, Y. Liu, R. Ma and W. Ye, *Chem. Eng. J.*, 2023, **451**, 138818.
17. M. Shen, W. Jiang, K. Liang, S. Zhao, R. Tang, L. Zhang and J.-Q. Wang, *Angew. Chem. Int. Ed.*, 2021, **60**, 27013-27018.

18. J. Zhao, J. Wen, J. Xiao, X. Ma, J. Gao, L. Bai, H. Gao, X. Zhang and Z. Zhang, *J. Energy Chem.*, 2021, **53**, 387-395.
19. P. Zhang, H. Shou, Y. Xia, C. Wang, S. Wei, W. Xu, Y. Chen, Z. Liu, X. Guo, K. Zhu, Y. Cao, X. Wu, S. Chen and L. Song, *Nano Lett.*, 2023, **23**, 1401-1408.
20. M. Li, J. Lu, K. Luo, Y. Li, K. Chang, K. Chen, J. Zhou, J. Rosen, L. Hultman, P. Eklund, P. O. Å. Persson, S. Du, Z. Chai, Z. Huang and Q. Huang, *J. Am. Chem. Soc.*, 2019, **141**, 4730-4737.
21. Y. Xie, X. Xiong and K. Han, *Ionics*, 2021, **27**, 3373-3382.
22. D. Sun, M. Wang, Z. Li, G. Fan, L.-Z. Fan and A. Zhou, *Electrochem. Commun.*, 2014, **47**, 80-83.
23. R. Cheng, T. Hu, H. Zhang, C. Wang, M. Hu, J. Yang, C. Cui, T. Guang, C. Li, C. Shi, P. Hou and X. Wang, *J. Phys. Chem. C*, 2019, **123**, 1099-1109.
24. T. Zhang, L. Chang, X. Zhang, H. Wan, N. Liu, L. Zhou and X. Xiao, *Nat Commun.*, 2022, **13**, 6731.
25. L. Huang, T. Li, Q. Liu and J. Gu, *Electrochem. Commun.*, 2019, **104**, 106472.
26. Q. Zhao, Q. Zhu, J. Miao, P. Zhang, P. Wan, L. He and B. Xu, *Small*, 2019, **15**, 1904293.
27. X. Song, H. Wang, S. Jin, M. Lv, Y. Zhang, X. Kong, H. Xu, T. Ma, X. Luo, H. Tan, D. Hu, C. Deng, X. Chang and J. Xu, *Nano Res.*, 2020, **13**, 1659-1667.
28. F. Kong, X. He, Q. Liu, X. Qi, Y. Zheng, R. Wang and Y. Bai, *Electrochim. Acta*, 2018, **265**, 140-150.
29. L. Liu, M. Orbay, S. Luo, S. Duluard, H. Shao, J. Harmel, P. Rozier, P.-L. Taberna and P. Simon, *ACS Nano*, 2022, **16**, 111-118.
30. V. Ghanooni Ahmadabadi, M. M. Rahman and Y. Chen, *Micromachines*, 2023, **14**, 191.